Prognostics Health Management of Electronic Systems Under Mechanical Shock and Vibration Using Kalman Filter Models and Metrics

Pradeep Lall, *Fellow, IEEE*, Ryan Lowe, and Kai Goebel

***Abstract*—Structural damage to ball grid array interconnects incurred during vibration testing has been monitored in the prefailure space using resistance spectroscopy-based state space vectors, rate of change of the state variable, and acceleration of the state variable. The technique is intended for condition monitoring in high reliability applications where the knowledge of impending failure is critical and the risks in terms of loss of functionality are too high to bear. Future state of the system has been estimated based on a second-order Kalman Filter model and a Bayesian Framework. The measured state variable has been related to the underlying interconnect damage in the form of inelastic strain energy density. Performance of the prognostic health management algorithm during the vibration test has been quantified using performance evaluation metrics. The methodology has been demonstrated on leadfree area-array electronic assemblies subjected to vibration. Model predictions have been correlated with experimental data. The presented approach is applicable to functional systems where corner interconnects in area-array packages may be often redundant. Prognostic metrics including $\alpha - \lambda$ precision, β accuracy, and relative accuracy have been used to assess the performance of the damage proxies. The presented approach enables the estimation of residual life based on level of risk averseness.**

***Index Terms*—Health monitoring, leading indicators of failure, prognostics, solder joint reliability.**

I. Introduction

HEALTH management in electronics high reliability applications primarily focuses on damage diagnosis involving built-in self-test to monitor for failure [1]–[6].

Damage diagnosis typically focuses on reactive failure detection and provides limited to no insight into the system reliability and residual life. Previously damage initiation, damage progression, and residual life in the prefailure space have been correlated with microstructural damage-based proxies, feature vectors based on time, spectral and joint time-frequency characteristics of electronics [7]–[18]. Precise resistance measurements based on the resistance spectroscopy method have been used to monitor interconnects for damage and prognosticate failure [19]–[24]. Avionics systems require ultrahigh reliability to fulfill critical roles in autonomous aircraft control and navigation, flight path prediction and tracking, and self-separation. Complex electrical power systems (EPS), which broadly comprise of energy generation, energy storage, power distribution, and power management, have a major impact on the operational availability and reliability of electronic systems. Technology trends in evolution of avionics systems pointtoward more electric aircraft [25] and the prevalent use of powersemiconductor devices in future aircraft and space platforms.Advanced health management techniques for electrical powersystems and avionics systems are required to meet the safety, reliability, maintainability, and supportability requirements ofaeronautics and space systems. Current health management techniques in EPS and avionics systems provide very limited or no visibility into health of power electronics packaging to predict impending failures [26]–[30].

Maintenance has evolved over the years from corrective maintenance to performing time-based preventive maintenance. Future improvements in reduction of system downtime require emphasis on early detection of degradation mechanisms. Incentive for development of prognostics and health management methodologies has been provided by need for reduction in operation and maintenance process costs [31]. Advances in sensor technology and failure analysis have catalyzed a broadening of application scope for prognostic systems to include large electromechanical systems such as aircraft, helicopters, ships, power plants, and many industrial operations. Current prognostic health management (PHM) application areas include fatigue crack damage in mechanical structures such as those in aircraft [32], surface ships [33], civil infrastructure [34], motors [35], motors [36], [37], hybrid electric vehicles [38], hydraulic actuator [39], railway structures [40], and power plants [31].

Kalman filtering is a recursive algorithm that estimates the true state of a system based on noisy measurements [41], [42]. Previously, the Kalman filter has been used for navigation [43], economic forecasting [44], online system identification [45], [46], and feedback control [47]. Typical navigation examples include tracking [48], ground navigation [49], altitude and heading [50], auto pilots [51], dynamic positioning [52], and GPS/INS/IMU guidance [53]. Application domains include GPS, missiles, satellites, aircraft, air traffic control, and

Manuscript received October 30, 2010; revised March 30, 2011, August 3, 2011, and November 7, 2011; accepted December 13, 2011. Date of publication January 23, 2012; date of current version June 19, 2012. This work was supported by NASA-IVHM Program Grant NNA08BA21C from the National Aeronautics and Space Administration.

P. Lall is with the Department of Mechanical Engineering, NSF-CAVE3 Electronics Research Center, Auburn University, Auburn, AL 36849 USA (e-mail: lall@auburn.edu).

R. Lowe is with the Department of Mechanical Engineering, Auburn University, Auburn, AL 36849 USA (e-mail: rdl0006@auburn.edu).

K. Goebel is with the NASA Ames Research Center (e-mail: kai.f.goebel@nasa.gov).

Color versions of one or more of the figures in this paper are available online at http://ieeexplore.ieee.org.

Digital Object Identifier 10.1109/TIE.2012.2183834

TABLE I
PACKAGE ARCHITECTURES USED FOR TEST BOARD

	6 mm Tape Array	7 mm Chip Array	10 mm Tape array	15 mm PBGA	16 mm Flex BGA	27 mm PBGA
I/O	64	84	144	196	280	676
Pitch (mm)	0.5	0.5	0.8	1	0.8	1
Die Size (mm)	4	5.4	7	6.35	10	6.35
Substrate Thick (mm)	0.36	0.36	0.36	0.36	0.36	0.36
Pad Dia. (mm)	0.28	0.28	0.30	0.38	0.30	0.38
Substrate Pad	NSMD	NSMD	NSMD	SMD	NSMD	SMD
Ball Dia. (mm)	0.32	0.48	0.48	0.5	0.48	0.63

ships. The ability of a Kalman filter to smooth noisy data measurements is utilized in gyros, accelerometers, radars, and odometers. Prognostication of failure using Kalman filtering has been demonstrated in steel bands and aircraft power generators [54]–[56]. Numerous applications in prognostics also exist for algorithms using more advanced filtering algorithms, known as particle filters. The state of charge of a battery was estimated and remaining useful life (RUL) was predicted in [57], [58]. Use of Kalman filtering for prognostication of electronic reliability based on the underlying damage mechanics is new. The Kalman filter has been utilized for this work since it is a robust tool for real-time tracking of noisy signals, with a long history of successful implementation. In this paper, a prognostic and health monitoring capability for electrical components based on changes in resistance has been presented. The presented PHM framework enables the estimation of RUL in deployed electronics by interrogation of the system state and evolution of the state vector. The methodology has been demonstrated on area-array package board assemblies subjected to mechanical shock and vibration. Failure modeling of ball grid array (BGA) interconnects is combined with Kalman filtering for plastic strain state estimation and a Bayesian framework for PHM. Prognostics metrics have been used to quantify the degree of uncertainty in the estimated RUL.

II. TEST VEHICLE

A set of test boards with multiple package architectures were used for experimental measurements. The test board includes package architectures such as plastic ball-grid arrays, chip-array ball-grid arrays, tape-array ball-grid arrays, and flex-substrate ball-grid arrays. The experimental matrix has ball counts in the range of 64 to 676 I/O, pitch sizes are in the range of 0.5 mm to 1 mm, and package sizes are in the range of 6 mm to 27 mm. The package parameters of this board are shown in Table I. Representative sample of the test board is shown in Fig. 1.

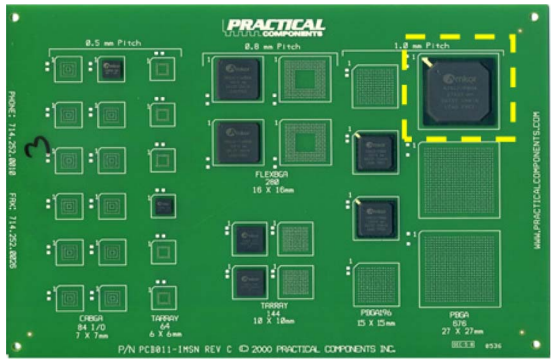

Fig. 1. Test board.

III. TEST CONDITIONS

The test assemblies were mounted face down on a Lansmont Model 23 drop tower (Fig. 2) and subject to a 0.5 millisecond, 1500 g impact pulse in accordance with JEDEC standard JESD-B211. Continuity for damage detection was done during the drops. Electrical continuity was monitored at 10 million samples per second during the test. High-speed digital video for use with digital image correlation software was also recorded during the drop test. The boards were subjected to resistance spectroscopy including both magnitude and phase-shift measurements between drops.

Phase shift measurements were repeated between drops until all packages on the board failed. The packages show varying degrees of damage when electrical continuity failures occur. Each package is interrogated by the resistance spectroscopy technique individually. Switching has been used to cycle through all the packages on the test board.

In addition to shock, the test assemblies were subjected to vibration testing on a LDS Model V722 vibration table. A step stress profile was used to gradually ramp up the stress level to induce damage (Fig. 3). The individual random stress profiles used in the step stress are shown in Fig. 4. The next section

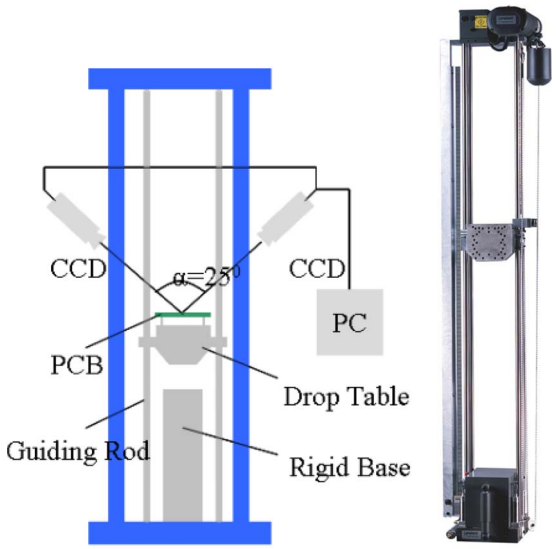

Fig. 2. (a) Drop tower and high speed digital cameras for digital image correlation. (b) Lansmont model 23 shock test system.

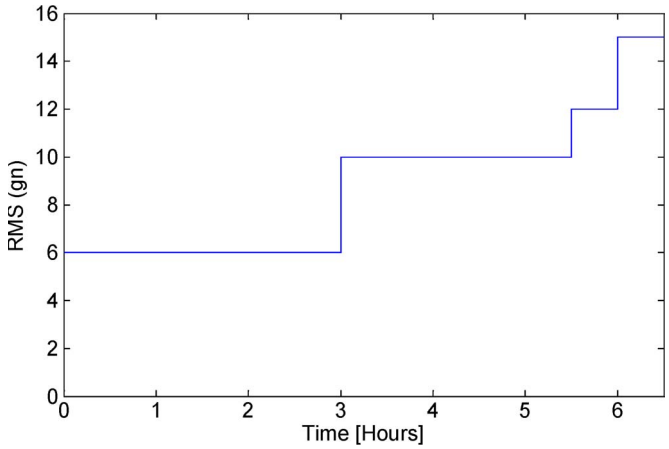

Fig. 3. Step stress profile for vibration testing that fatigues interconnects to failure.

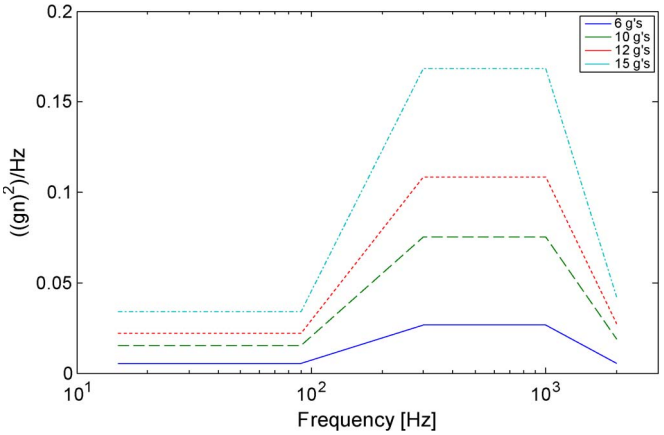

Fig. 4. Random vibration profile at varying g levels corresponding to the step stress profile outlined in Fig. 4.

will discuss how the transient response of a package during random vibration testing was monitored for a leading indicators of failure.

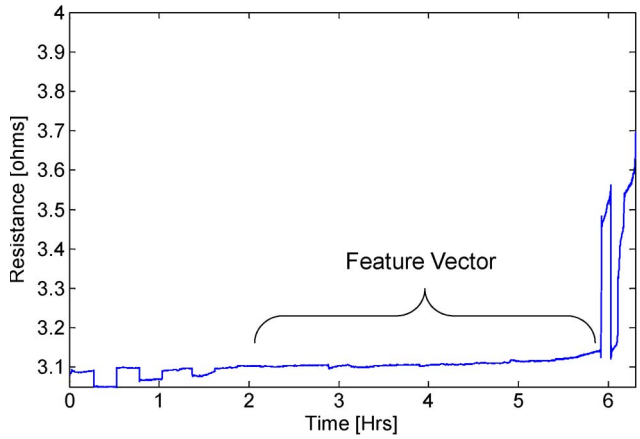

Fig. 5. Raw resistance data. The data used as an input data vector is shown in the brackets.

IV. Transfer Function for Interconnect Strain to Resistance

The daisy chained resistance of a package was used as a leading indicator of failure in this paper. The observed history of the resistance of the package during vibration testing is shown in Fig. 5. At approximately 5.8 h, the package experiences its first intermittent open event. In the following plots, large resistance values have been truncated for clarity.The resistance of an open event of 300 Ω or more makes it difficult to discuss mili-ohm changes on a plot. The resistance of the daisy chained package was recorded using an Agilent 34970A data acquisition unit with a two wire resistance measurement setup. Measurements were taken at a frequency of 0.2 Hz. Since data measurements were recorded every few seconds, but the test lasted for approximately 6 h, this was deemed to be an effectively high sampling frequency to capture trends in the leading indicator of failure. The impact of decreasing the sampling frequency to optimize the computational efficiency of the prognostic algorithms has not been studied, but would be valuable for future work. Additional details quantifying the applicability of the measurement system for capturing intermittent events in advance of the traditional definition of failure can be found in [21].

The failure criteria for resistance change outlined in industry standards JESD22-B103 [5], and IPCSM785 [4]for the number, duration, and severity of intermittent events are used as the definition of failure. It should be noted that the smaller step increases of 0.05 Ω during the first 90 min of the test are experimental noise which can be reproduced by motion of the system connections during shock and vibration. Resistance data 2 h after the initiation of the test till failure has been studied for the construction of a feature vector for identification of impending failure. A subset of the resistance data has been used since field data will often involve electronic assemblies with accrued damage and not involve pristine assemblies. Fig. 6 shows a zoomed view of the input data highlighting the experimental noise between 2 h and failure. The experimental noise is due in part to the challenges with overcoming the variance in contact resistance in the presence of transient dynamic motion in shock or steady-state vibration. Step changes in the resistance data can be seen at 2.8 and 4.9 h, respectively. However, the distinctive

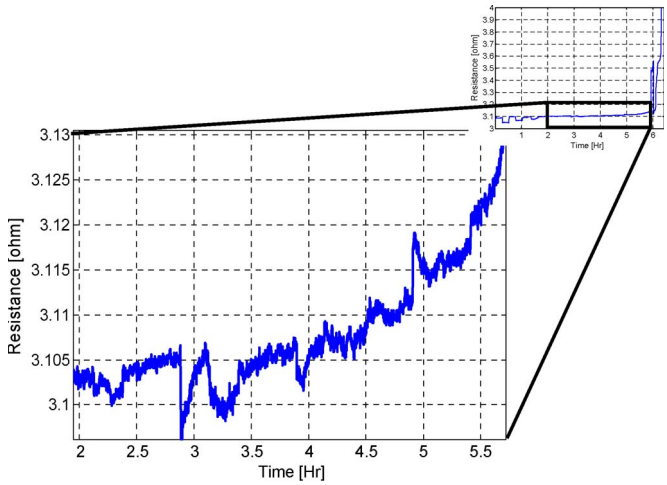

Fig. 6. Zoomed view of resistance data between 2 h and failure.

TABLE II
ANAND'S CONSTANTS FOR SAC305

S_o	45.9 MPa
Q/K	7460 1/K
A	5.87e6 1/sec
ξ	2
M	0.0942
h_o	9350 MPa
n	0.015
a	1.5
s	58.3 MPa

increase of about 25 mΩ during the vibration test is easily discernible even in the presence of experimental noise.

The change in resistance is attributed to change in geometry, since the resistivity of the solder interconnect is expected to stay constant. Change in trace geometry is the basis of operation for traditional strain gages and can be explained in a cylindrical conductor by $R = \rho L/A$, where R is the resistance of the conductor, ρ is the material property resistivity, L is length and A is the cross-sectional area. By logarithmically differentiating both sides and assuming linear elastic properties, a relation between strain and resistance can be derived as $dR = R_0\varepsilon_a(1 + 2\nu)$, where dR is the change in resistance, R_0 is the initial resistance, ε_a is the elastic axial strain, and ν is the Poisson ratio. Since the material properties and geometry of a solder ball are nonlinear, a finite-element simulation (FEM) was used to map the change in resistance of an interconnect to the state of plastic strain that the interconnect was feeling. The simulation was implemented in ANSYS Version 12 using Anand's Viscoplasticity and VISCO107 elements. The Anand's constants used for the simulation are shown in Table II.

Table III shows the dimensional parameters for the undeformed geometry of a typical solder ball based on the manufacture's data sheet. Previous studies have shown that tensile stress in the out-of-plane z-direction is the primary stress during the shock test in the solder interconnects [59], [60]. The solder interconnect deformation during the shock test was simulated using nonlinear finite elements by constraining the solder interconnect along the bottom of the joint and applying a displacement load on the top (Fig. 7).

TABLE III
UNDEFORMED GEOMETRY OF SOLDER BALL

Parameter	Specification
Solder ball diameter (mm)	0.63
Solder ball land (mm, board and package)	0.45
Solder ball height after reflow (mm)	0.48

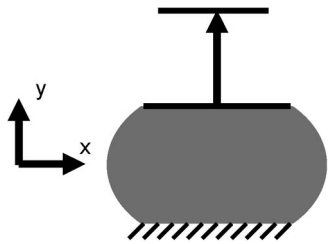

Fig. 7. Constraints on solder ball for FEM simulation.

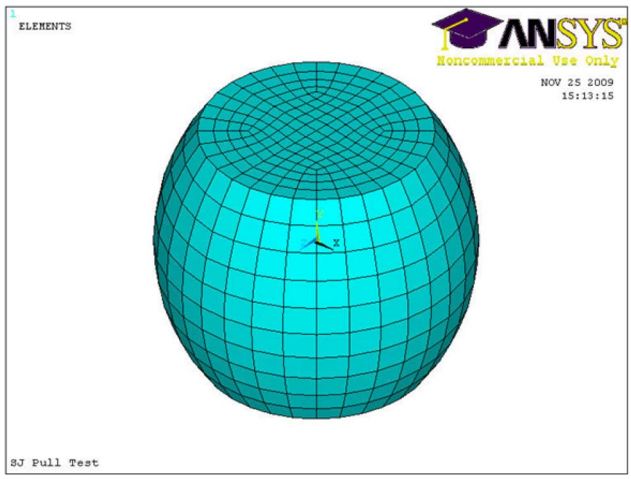

Fig. 8. Meshed model of solder ball.

Resistance of the solder interconnect was computed by converting the VISOC107 elements to SOLID5 elements after intermediate steps in the deformation. A steady-state conductance simulation was run using the deformed geometry after each substep. Using the built-in macrocommand GMATRIX, the conductance of the solder ball in the deformed state could be calculated. The conductance is the inverse of the resistance. The meshed geometry before deformation can be seen in Fig. 8, while the deformed geometry can be seen in Fig. 9. Deformation was applied to the solder joint at a specified strain rate of 1 s^{-1} typical of a shock test. An example of this mapping is shown in Fig. 10.

Following a method similar to [8] and [59] the assumed criteria for failure in the simulated solder joint was based on the joint exceeding a critical plastic strain value. The critical plastic strain value was determined from a BGA pull test. Based on the experimental data at a strain rate of 1/s, an overall strain of the

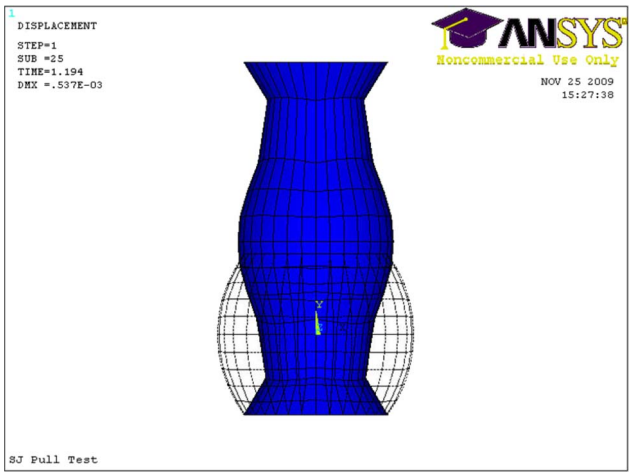

Fig. 9. Deformed and undeformed geometry of solder ball.

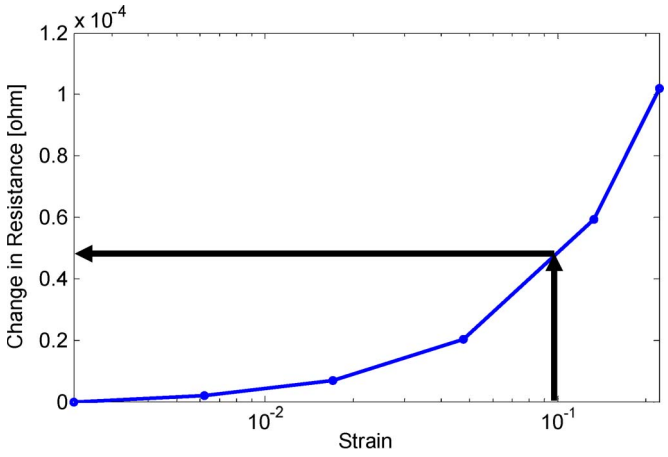

Fig. 10. Simulated change in resistance of solder ball during pull test. Arrows indicate expected change in resistance at a strain of 0.1.

solder joint of 0.1 corresponded to failure. Model predictions indicate a change in resistance of $5 \times 10^{-5}\ \Omega$ correlates with interconnect strain of 0.1 prior-to-failure of the interconnect. This critical resistance value derived from the FEM simulation will be used as a threshold value to define failure for the PHM algorithm. Since the daisy chained resistance of a package is monitored in this study the critical resistance calculated from the FEM simulation must be scaled up from a single solder ball to account for changes in resistance of the entire package. This was achieved by approximating that every interconnect feels the same strain. Therefore, the critical resistance is multiplied by the number of I/O in the package, i.e., 676 for the PBGA 676 to obtain the overall critical resistance value $(676 \times 5 \times 10^{-5}\ \Omega = 3.38 \times 10^{-2}\ \Omega)$. Assuming that every interconnect feels the same strain is not strictly correct since failure most often occurs in the corner interconnects. This implied averaging of strain across all interconnects is justified since deflections were small for the vibration test. Ultimately, errors from this approximation add uncertainty to the RUL calculation. As will be demonstrated later in the paper, this uncertainty must be managed to obtain meaningful results.

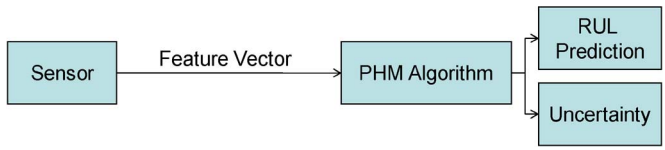

Fig. 11. Flowchart for PHM framework.

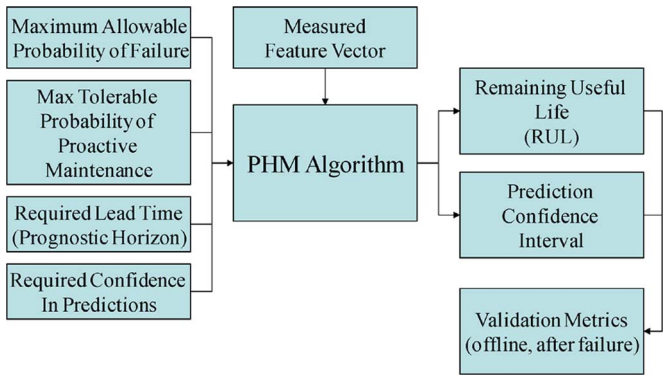

Fig. 12. Inputs and outputs to PHM algorithm.

V. PHM Framework

The strain-resistance relationships have been used to correlate the measured feature vector with the underlying damage state of the system. Feature vectors monitoring system damage have been constructed based on the sensor output (Fig. 11). The feature vector is an input into the PHM algorithms.

Previous researchers have investigated various PHM frameworks for assessment of accrued damage and estimation of RUL. Examples include model or physics of failure-based methods [7]–[22], statistical trending [31], artificial intelligence-based prognostics [62], and state estimator methods [54]–[56]. In this paper, a Bayesian framework has been used [57], [58], [64], [65] to allow statistically defendable decisions to be made based on the RUL predictions using the PHM algorithm. The probability that a flaw (F) exists given a positive indication (I) depends on sensor's probability of detection given that a flaw exists $P(I|F)$, probability of false alarm $P(I| \sim F)$, and prior probability that the flaw exists before any measurements are made P(F)

$$P(F|I) = \frac{P(I|F)P(F)}{P(I)} = \frac{P(I|F)P(F)}{P(I|F)P(F) + P(I| \sim F)P(\sim F)} \quad (1)$$

where the prefix "$\sim$" is used to represent "not," $P(I| \sim F)$ is the probability of detection if when the flaw does not exist, and $P(\sim F)$ is the probability of the nonexistence of a flaw.

The PHM algorithm used in this study requires four inputs from the user prior to operation (Fig. 12).

1) Maximum allowable probability of failure.
2) Maximum tolerable probability of proactive maintenance.
3) Required lead time to receive a replacement component.
4) Required confidence in the RUL predictions.

The PHM algorithm outputs the RUL at every point that a measurement is made, and the accompanying confidence

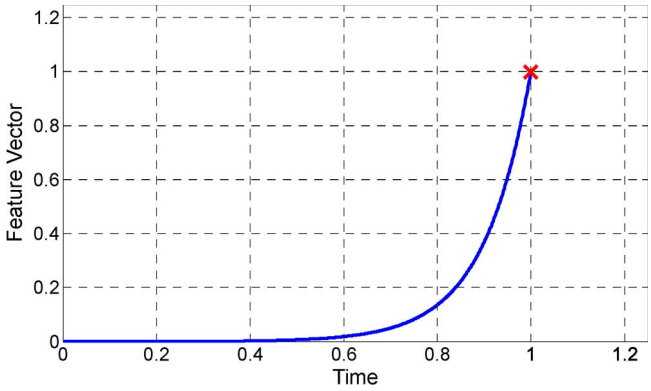

Fig. 13. Generalized shape of feature vector for prognosticating failure.

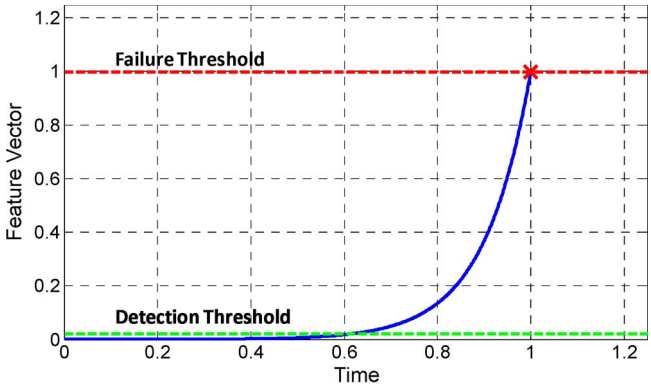

Fig. 14. Detection and failure thresholds for feature vector.

interval around the RUL prediction. The RUL prediction, coupled with the confidence interval allows statistically defendable decisions to be made concerning the future use and maintenance of the system being monitored. The performance of the algorithm is validated offline after failure of the component. Fig. 13 generalizes the shape of a typical feature vector. The details of a feature vector for a system can be application specific; therefore, a normalized value of one for the feature vector is defined as system failure. A typical feature vector can be very nonlinear in nature, particularly toward the end of life. Initial measurements often involve a period where no noticeable change in the feature vector can be detected. Accrued damage in the system will shift the feature vector over time and cause it to cross the detection threshold as shown in Fig. 14. The component is defined as failed when the feature vector breaks the failure threshold.

In the Bayesian framework, all predictions have an associated uncertainty. The uncertainty has been assumed to be Gaussian in nature, and the probability density function (PDF) of the predicted time of failure computed. Fig. 15 illustrates how the mean value of the predicted time to failure, represented as a probability distribution, is before the actual failure indicated with an "x." Prediction error and uncertainty are discussed in more detail in Section VIII. The shaded region in Fig. 16 represents the area under the PDF curve that is equal to the maximum allowable probability of failure. Furthermore, the maximum tolerable probability of proactive maintenance can be unshaded to represent the window of opportunity that will

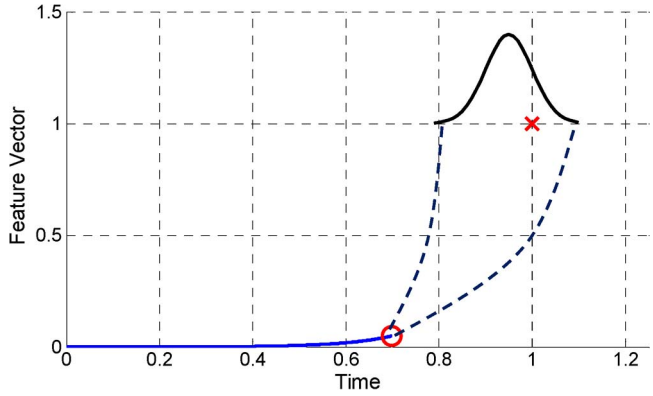

Fig. 15. Prediction of failure at time $= 0.7$.

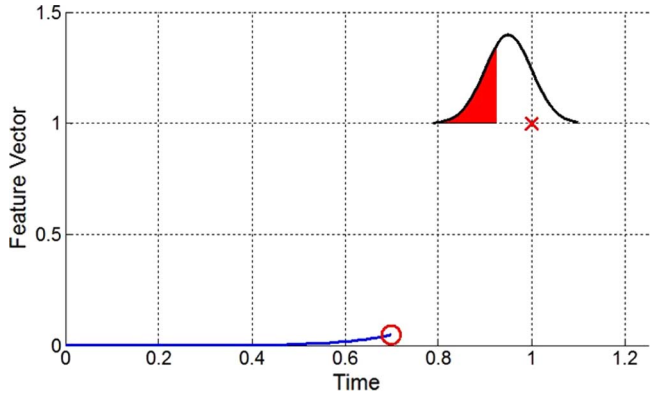

Fig. 16. Maximum allowable probability of failure (red shaded region).

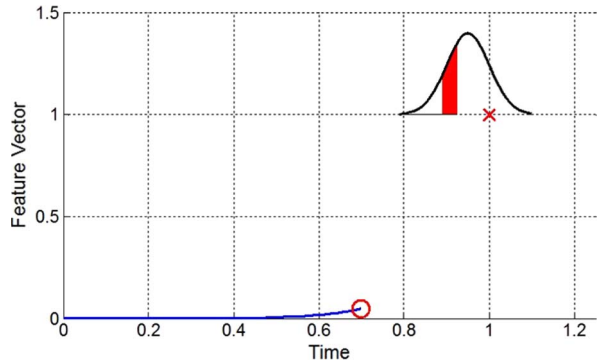

Fig. 17. Window of opportunity for repair or replacement based on RUL prediction at time $= 0.7$.

still meet all of the specified criteria specified by the user as shown in Fig. 17.

Fig. 17 shows the window of opportunity to replace the component based on a prediction at time $= 0.7$. The estimate of time-to-failure and the RUL is updated at the next time step. Fig. 18 shows the updated probability distribution function for the system at time step $t = 0.9$. In system prognostication, the estimate of system failure is updated at every time step as new information becomes available. The Kalman filter has been used to track the state of the noisy feature vector. The output from the Kalman filter is an estimate of the damage state of the BGA solder interconnect. The future system states are predicted based on the previous state-vectors, process noise, measurement noise, system dynamics matrix, and the measurement

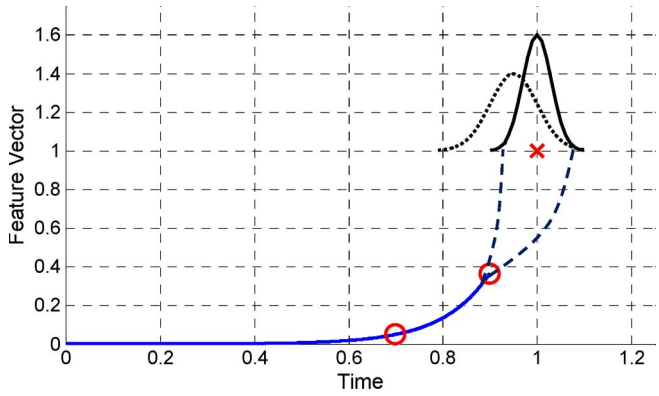

Fig. 18. Updated RUL prediction at time = 0.9.

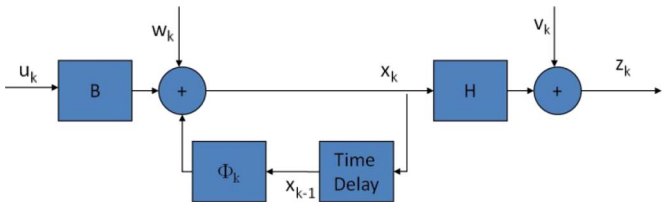

Fig. 19. Graphical state space representation of a system.

matrix using the second-order Kalman filter until the feature vector exceeds the threshold value. Since the Kalman filter is a recursive algorithm, only one measurement of the feature vector is stored at one time.

VI. Filtering and RUL Prediction

System damage state estimation in the presence of measurement noise and process noise has been achieved using the Kalman Filter. Previously, the Kalman Filter has been used in guidance and tracking applications [41], [42]. System state has been described in state space form using the measurement of the feature vector, the velocity of feature vector change and the acceleration of the feature vector change. System state at each future time has been computed based on the state space at the preceding time step, system dynamics matrix, control vector, control matrix, measurement matrix, measured vector, process noise, and measurement noise. Fig. 19 represents the data flow through the system, where u_{k} is the control vector or input for the system, w_{k} is process noise, x_{k} is the state space vector at the kth time step, H is the measurement matrix which is a constant in this implementation, v_{k} is the measurement noise, z_{k} the measured state, and Φ_{k} is the system dynamics matrix.

The equivalent Kalman Filter equation for state space representation in the presence of process noise and measurement noise is:

$$\hat{x}_{\mathrm{k}} = \Phi_{\mathrm{k}}\hat{x}_{\mathrm{k-1}} + B_{\mathrm{k}}u_{\mathrm{k-1}} + K_{\mathrm{k}}(z_{\mathrm{k}} - H\Phi_{\mathrm{k}}\hat{x}_{\mathrm{k-1}} - HB_{\mathrm{k}}u_{\mathrm{k-1}}) \quad (2)$$

$$z_{\mathrm{k}} = Hx_{\mathrm{k}} \quad (3)$$

where $\hat{x}_{\mathrm{k}}$ is the Kalman Filter estimate of system state at time kth time step,x_{k} is the actual system state at the kth time step, and B_{k} is the control vector. The Kalman gain has been computed and updated at each time step, while the filter is operating from the Riccati equations [42]. The Ricatti equations can be represented in matrix form as:

$$M_{\mathrm{k}} = \Phi_{\mathrm{k}}P_{\mathrm{k-1}}\Phi_{\mathrm{k}}^{\mathrm{T}} + Q_{\mathrm{k}} \quad (4)$$

$$K_{\mathrm{k}} = M_{\mathrm{k}}H^{\mathrm{T}}(HM_{\mathrm{k}}H^{\mathrm{T}} + R_{\mathrm{k}})^{-1} \quad (5)$$

$$P_{\mathrm{k}} = (1 - K_{\mathrm{k}}H)M_{\mathrm{k}} \quad (6)$$

where M_{k} is the covariance of errors in state estimates before update, Φ_{k} is the fundamental matrix which represents the system dynamics, Q_{k} is the discrete process noise matrix, K_{k} is the Kalman gain, H is the measurement matrix, and P_{k} is the covariance matrix representing errors in the state estimate after an update. R_{k} is the process noise matrix and has been used as a device for telling the filter that we know that filter's model of the real world is not precise. The diagonal elements of P_{k} represent variance of the true state minus the estimated state. M_{k} is sometimes referred to as the a priori covariance matrix, and P_{k} may be referred to as the posterior covariance matrix.

The feature vector used for prognosis of the system health is not a constant or a straight line, therefore the zeroth and first order systems were ruled out and a second order system was used for representation of system state evolution with progression of underlying damage. The choice of the second order filter was also influenced by the general observation that feature vectors evolve nonlinearly and generally accelerate toward the end of life. The rate of evolution of a second-order system can be represented as follows:

$$\begin{Bmatrix} \dot{x} \\ \ddot{x} \\ \dddot{x} \end{Bmatrix} = [F] \begin{Bmatrix} x \\ \dot{x} \\ \ddot{x} \end{Bmatrix} = \begin{Bmatrix} 0 & 1 & 0 \\ 0 & 0 & 1 \\ 0 & 0 & 0 \end{Bmatrix} \begin{Bmatrix} x \\ \dot{x} \\ \ddot{x} \end{Bmatrix}. \quad (7)$$

The fundamental matrix has been computed from the Taylor series expansion of the system dynamics matrix, F, as follows:

$$\Phi(t) = e^{\mathrm{Ft}} = I + Ft + \frac{(Ft)^2}{2!} + \ldots + \frac{(Ft)^n}{n!} + \ldots$$

$$\Phi(t) = \begin{pmatrix} 1 & 0 & 0 \\ 0 & 1 & 0 \\ 0 & 0 & 1 \end{pmatrix} + \begin{pmatrix} 0 & 1 & 0 \\ 0 & 0 & 1 \\ 0 & 0 & 0 \end{pmatrix} t + \begin{pmatrix} 0 & 0 & 1 \\ 0 & 0 & 0 \\ 0 & 0 & 0 \end{pmatrix} \frac{t^2}{2!}$$

$$\Phi_{\mathrm{k}} = \Phi(T_{\mathrm{s}}) = \begin{pmatrix} 1 & T_{\mathrm{s}} & 0.5T_{\mathrm{s}}^2 \\ 0 & 1 & T_{\mathrm{s}} \\ 0 & 0 & 1 \end{pmatrix}. \quad (8)$$

Note that the F^3 terms and above are identically zero; therefore, the expansion only has three nonzero terms. A model based on the accrued plastic work in interconnects of the system has not been used because the inputs to the system are not always known or measurable and cannot be assumed to always be constant or known in advance. Therefore, the feature vector based on resistance spectroscopy has been related to the underlying plastic work and its evolution used for prognostication of system state and residual life. The first and second derivatives of the feature vector based on resistance spectroscopy have been computed to estimate the state of the feature vector at future time steps. The system state vector is represented as

$x_{\mathrm{k}} = \lfloor x\ \dot{x}\ \ddot{x} \rfloor^{\mathrm{T}}$, where x is the interconnect resistance of the daisy chained package, $\dot{x}$ is the ramp rate of the interconnect resistance, and $\ddot{x}$ is the second derivative with respect to time of the interconnect resistance. The state vector evolution is represented as follows:

$$\begin{Bmatrix} x_{\mathrm{k+1}} \\ \dot{x}_{\mathrm{k+1}} \\ \ddot{x}_{\mathrm{k+1}} \end{Bmatrix} = \begin{pmatrix} 1 & T_{\mathrm{s}} & 0.5T_{\mathrm{s}}^2 \\ 0 & 1 & T_{\mathrm{s}} \\ 0 & 0 & 1 \end{pmatrix} \begin{Bmatrix} x_{\mathrm{k}} \\ \dot{x}_{\mathrm{k}} \\ \ddot{x}_{\mathrm{k}} \end{Bmatrix}. \tag{9}$$

The uncertainty of each prediction was quantified using the posterior error covariance. As an engineering approximation, the uncertainty is calculated using a straight line approximation. Then, the uncertainty from the linear approximation is superimposed on the failure prediction obtained fromiteratively solving for the intersection of a quadratic equation with the critical resistance threshold. This is a trade off in accuracy, for the benefit of algorithm simplicity.

Assuming that the feature vector and its first derivative are normal random variables (Gaussian), then a straight line approximation of the time to failure can be

$$t_{\mathrm{f}} = \frac{x_{\mathrm{f}} - \hat{x}}{\dot{\hat{x}}} \tag{10}$$

where t_{f} is the time to failure, x_{f} is the failure threshold, $\hat{x}$ is the estimated state of the system (resistance) and $\dot{\hat{x}}$ is the estimate of the first derivative. The numerator will have a variance equal to the variance of the position estimate, which is directly available in the posterior error covariance matrix as P(1,1). The denominator will have a variance equal to the variance of the first derivative estimate, directly available as P(2,2). If

$$\sigma_{\mathrm{F}}^2 = P(1,1) \quad \sigma_{\mathrm{R}}^2 = P(2,2) \tag{11}$$

then it is demonstrated in [55] that the non-Gaussian distribution resulting from the ratio of two normal distributions with variances of σ_{F}^2 and σ_{R}^2 can be integrated to find the equivalent 68.4% probability range around the mean.

$$\sigma = 1.86\frac{\sigma_{\mathrm{F}}}{\sigma_{\mathrm{R}}}. \tag{12}$$

The mean of the distribution from the straight line approximation is disregarded since the more iterative method was used to solve for the intersection of the quadratic equation with the critical resistance threshold.

The uncertainty estimate around the RUL prediction includes a number of simplifying assumptions about the nature of the system and should only be taken as a rough estimate. It will be shown later that this metric is still useful in understanding the operation of the algorithm and is necessary for fully utilizing the PHM framework to make risk-based decisions.

The extrapolation of the estimated state into the future to determine the RUL was accomplished by using the state evolution equation to iteratively solve the intersection of a quadratic equation with the critical resistance threshold. The parameters of the quadratic equation are estimated from the Kalman filter.

The Kalman filter equations are recursive and must be initialized before the first measurement. The initial state estimate was taken as zero since the system is expected to have zero change

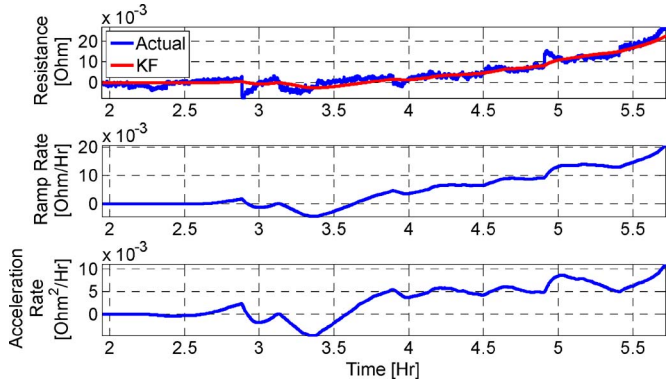

Fig. 20. Results of Kalman filtering.

in resistance before incurring damage. The measurement noise term was obtained from the observed variance in the measurement system during the first 30 s of testing ($R_{\mathrm{k}} = 5e-6$). The process noise term was taken as $Q_{\mathrm{k}} = 1e-9$ and represents the uncertainty in the process dynamics. The diagonals of the posterior error covariance matrix were setarbitrarily large to 1000, which indicates a complete lack of trust in the initial state estimate.The filtering and prediction algorithm is summarized below.

Algorithm: Filtering and RUL Prediction

1) Initialize variables at time step $t = 0$.
2) Project state at the next time step, $x_{\mathrm{k}} = \Phi_{\mathrm{k}} x_{\mathrm{k-1}}$.
3) Calculate error covariance before update, $M_{\mathrm{k}} = \Phi_{\mathrm{k}} P_{\mathrm{k-1}} \Phi_{\mathrm{k}}^{\mathrm{T}} + Q_{\mathrm{k}}$.
4) Calculate Kalman gain, $K_{\mathrm{k}} = M_{\mathrm{k}} H^{\mathrm{T}} (H M_{\mathrm{k}} H^{\mathrm{T}} + R_{\mathrm{k}})^{-1}$.
5) Take measurement, $z_{\mathrm{k}} = H x_{\mathrm{k}}$.
6) Update estimate with measurement, $\hat{x}_{\mathrm{k}} = \Phi_{\mathrm{k}} \hat{x}_{\mathrm{k-1}} + K_{\mathrm{k}}(z_{\mathrm{k}} - H \Phi_{\mathrm{k}} \hat{x}_{\mathrm{k-1}})$.
7) Calculate error covariance after measurement update, $P_{\mathrm{k}} = (1 - K_{\mathrm{k}} H) M_{\mathrm{k}}$.
8) Extrapolate feature vector many time steps, n, to the failure threshold value, $x_{\mathrm{k+n}} = \Phi_{\mathrm{k+n}} x_{\mathrm{k+n-1}}$.
9) Report predicted RUL (and uncertainty).
10) Iterate to step 2) for next measurement $(k = k + 1)$.

VII. Estimation of Remaining Useful Life

The Kalman filter tracking results used for prognostication are shown in Fig. 20. The measured data have been obtained from resistance spectroscopy. The red line in the first plot is the state estimate from the Kalman filter. Note that the state estimate from the Kalman Filter is smoother than the raw data-based feature vector. Smoothing facilitates faster convergence in the PHM algorithm. The lower two plots are estimates of the first and second derivative of the field quantity measured for construction of the feature vector. Any time the velocity is negative, the PHM algorithm cannot make a prediction. This causes the RUL predictions to oscillate before convergence. The convergence of the Kalman gain is shown in Fig. 21.

The Newton-Raphson's method has been used for calculation of the RUL. A threshold value of 1×10^{-6} has been used as the

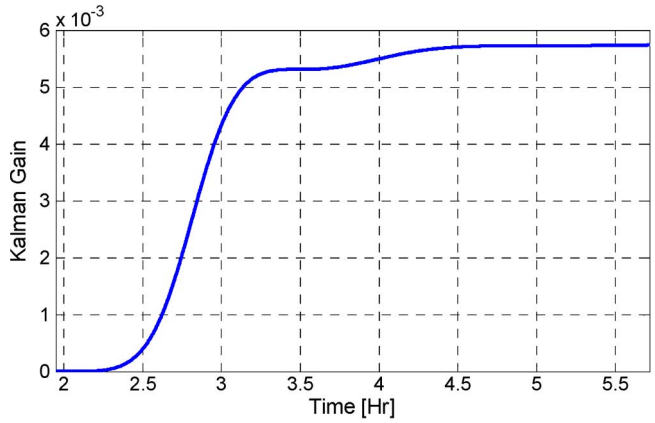

Fig. 21. Convergence of the Kalman gain for the resistance estimate term.

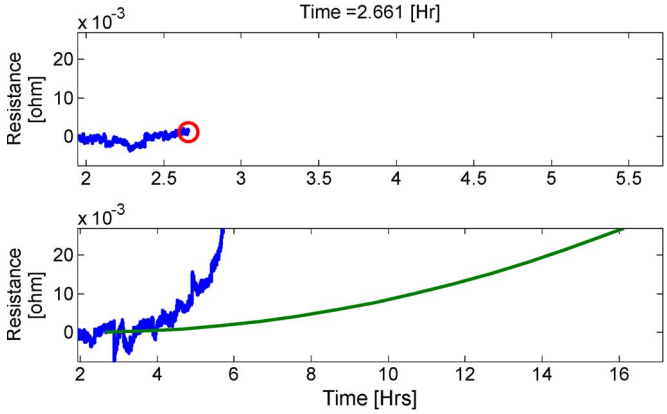

Fig. 22. RUL prediction at 2.6 h, the red circle shows what data was available for the prediction. The blue line in both plots is the feature vector, and the green line is the extrapolated state value used to predict RUL.

threshold for convergence

$$t_{n+1} = t_n - \frac{f(t)}{f'(t)} \tag{13}$$

$$t_{fn+1} = t_{fn} - \frac{x_0 + \dot{x}t_{fn} + \frac{1}{2}\ddot{x}t_{fn}^2 - x_f}{\dot{x} + \ddot{x}t_{fn}} \tag{14}$$

where $f(t) = x_0 + \dot{x}t_{fn} + \frac{1}{2}\ddot{x}t_{fn}^2 - x_f$, x is the state variable in the state space vector, t_{fn} is the estimate of the failure time at the time step n, and x_f is the failure threshold for the state variable. The estimate of the failure time is updated in accordance with evolution of state-space vector which correlates with the underlying damage.

The results of the RUL prediction are shown in Figs. 22–24. Fig. 22 is a prediction from early in the test. Based on the data available, which shows very little change in the state variable resistance, the RUL prediction is considerably longer than the actual RUL. Fig. 23 shows a prediction where more information is available to the algorithm. In Fig. 24, a prediction at the very end of the test shows the measured feature vector increasing in an exponential nature. The use of a quadratic model for predicting future states many time steps into the future was adequate for most of the test, but results in a prediction error at the extreme end of the test where failure propagation is highly nonlinear. A higher order model or a nonlinear model

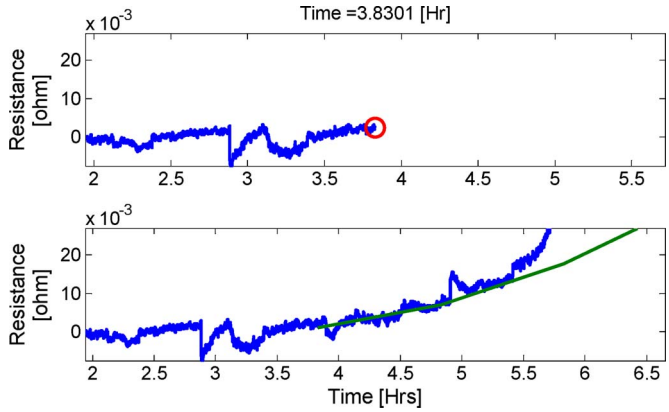

Fig. 23. RUL prediction at 3.8 h.

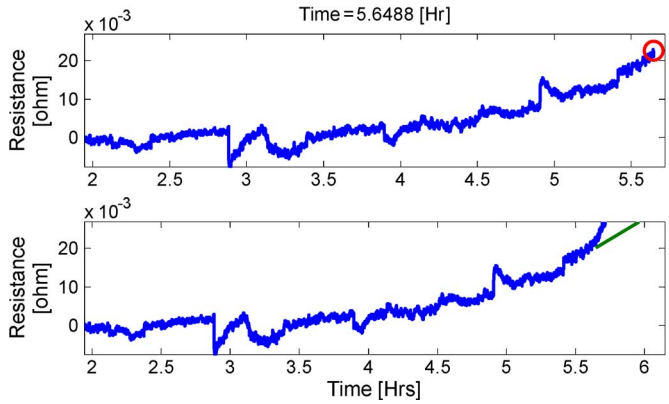

Fig. 24. RUL prediction at 5.6 h.

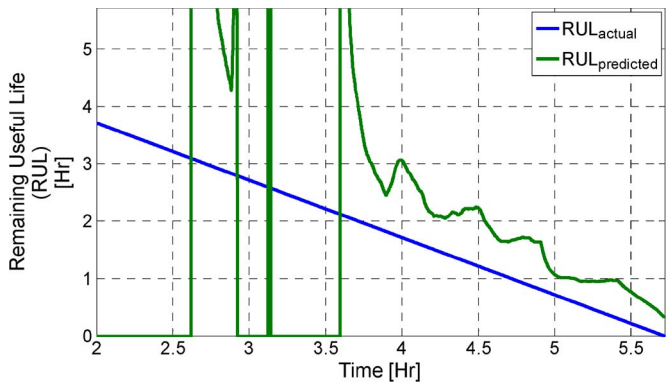

Fig. 25. Comparison of actual RUL versus predicted RUL.

(implemented with an extended Kalman filter [22]) may provide better tracking and performance near the end of life, at the cost of implementation complexity. Section VIII describes a quantitative method for evaluating and comparing the choice of model or algorithm based on prediction performance metrics. Using the performance metrics, design decisions could be made to continue developing better system models, or to consider the error as an acceptable engineering approximation. A summary of all the RUL predictions compared against the actual RUL is shown in Fig. 25. The initial estimates of the RUL oscillate and then gain traction in terms of accuracy following evolution of state space vector with underlying damage.

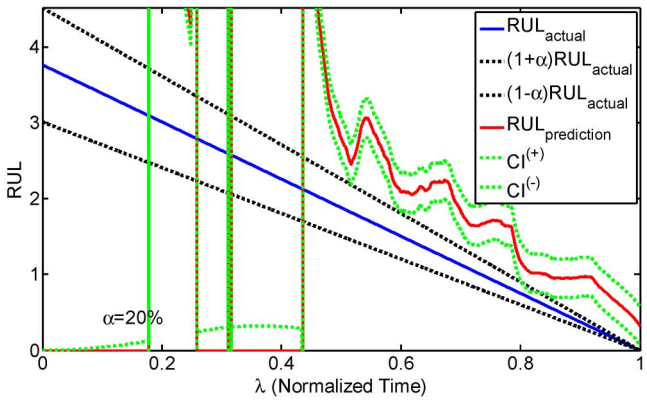

Fig. 26. Alpha-Lambda performance of PHM Algorithm.

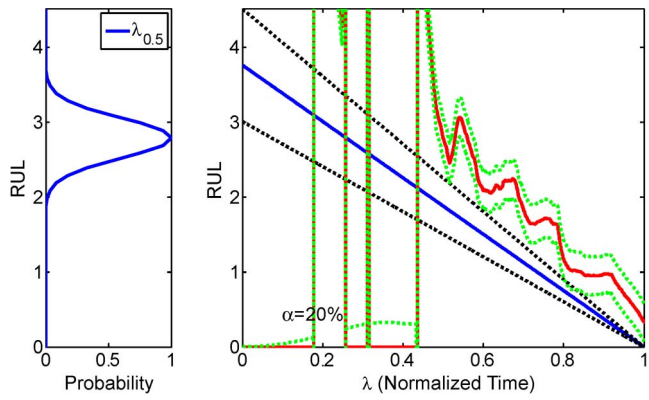

Fig. 27. Probability density function for RUL prediction at lambda = 0.5.

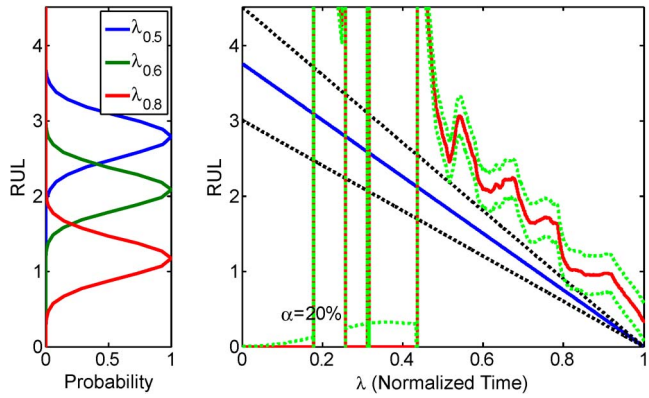

Fig. 28. RUL prediction PDF at lambda = 0.5, 0.6, 0.8.

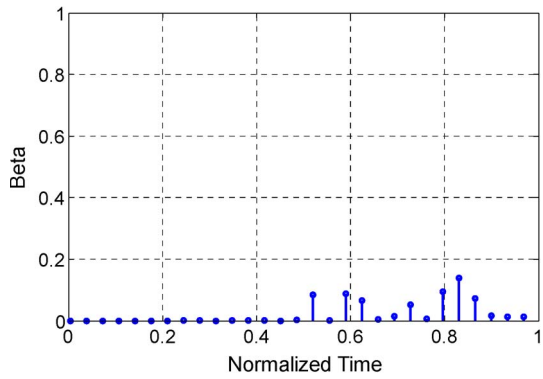

Fig. 29. Beta calculation showing area under RUL prediction PDF that falls within the alpha bounds.

VIII. Prognostics Metrics

The experimental value of time to failure is known after completion of the accelerated test. A comparison of the actual life of the component versus the predicted life has been calculated to quantify and validate the PHM algorithm. The validation process follows the algorithm assessment metrics proposed in [66]–[69].

The validation method shown here is a four-step process. First the alpha-lambda performance has been calculated to determine the time over which the algorithm successfully predicted the RUL. Then, the beta statistic is calculated to quantify the precision of the RUL predictions. Next, the relative accuracy is calculated, and finally the convergence of the algorithm is calculated. Each metric will be briefly discussed using the experimental results from the previous section. A full treatment of the validation metrics is included in the original references.

The alpha-lambda metric, shown in Fig. 26, compares the actual RUL against the predicted RUL. The actual RUL can only be calculated after the component has been stressed to failure. The alpha bounds are application specific. They provide a goal region for the algorithm at $\pm(\alpha)(100)\%$ of the actual RUL. If the predicted RUL falls within the alpha bounds, then it is counted as a correct prediction. The alpha bounds are not the uncertainty bounds for predicted RUL which indicate the uncertainty in the predicted RUL. Lambda is defined as the normalized time and is calculated as $\lambda = (t - t_o/t_f)$, where t is the present time, $t_{\rm o}$ is the detection time, and $t_{\rm f}$ is the final time of failure. A normalized time of zero represents the beginning of the test, while at a normalized time of one the component has failed. Normalized time is plotted on the x-axis and facilitates the comparison of components that fail at different times. Fig. 27 shows the PDF for the RUL prediction at lambda = 0.5. Fig. 28 shows multiple PDF's overlaid from RUL predictions at different times.

The second metric, the beta calculation, is defined as the area under the predicted RUL PDF that falls within the alpha bounds at the specified normalized time, λ. Symbolically, this is represented as:

$$\beta = \int_{\alpha^{(-)}}^{\alpha^{(+)}} \phi(x)\, dx. \tag{15}$$

This metric discriminates against algorithms that have a lot of uncertainty associated with the RUL prediction. A high beta-value value indicates a superior RUL prediction. The beta metric can also be alternatively used in conjunction with the alpha-lambda plot to define when a prediction is successful. For example, an arbitrary beta value can be the threshold for making a correct RUL prediction. The beta calculation is shown in Fig. 29.

The third metric involves the calculation of the relative accuracy. Relative accuracy has a value of 1, in absence of error in the predicted value of RUL. Relative accuracy is defined as:

$$\mathrm{RA}_\lambda = 1 - \frac{|\mathrm{RUL}_{\rm actual} - \mathrm{RUL}_{\rm predicted}|}{\mathrm{RUL}_{\rm actual}}. \tag{16}$$

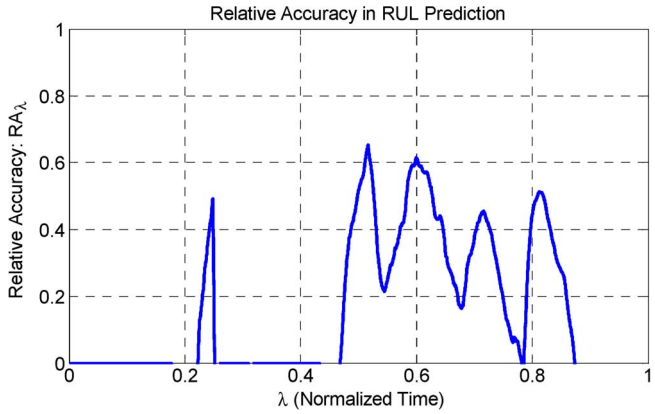

Fig. 30. Relative accuracy of RUL prediction.

Relative accuracy is used as a metric to emphasize that errors closer to the actual failure of a component are more severe, see Fig. 30. The peaks in Fig. 30 indicate higher accuracy.

In practice, prognostic metrics help to quantify the performance of the algorithm demonstrated in this paper and facilitate comparisons with other algorithms and methods. Each application domain will have a specific set of criteria to determine if the PHM capability is sufficient for inclusion into a larger system. The use of standardized prognostics metrics facilitates this comparison. For example by looking at the metrics from this paper, an accurate RUL prediction was made for a period of time, but there was a systemic error in the algorithm that consistently over predicted the RUL. Evaluating if the advanced warning of failure (prognostic distance) at a given accuracy level is sufficient can only be determined using application specific criteria in conjunction with the prognostic metrics.Hypothetically, a commercial off the shelf component, like studied in this paper, may see service in an aerospace vehicle, military jet, and commercial jet. The electrical component could experience similar vibration levels in each system. The application specific requirements for each system may differ drastically for the same component. In an aerospace vehicle, each mission can easily be delayed to ensure the ultimate mission success, while in a military or commercial scenario availability is much more crucial. The required prognostic performance would therefore be different for each application. Prognostic metrics provide a common yardstick for evaluating a PHM implementation against a specific set of requirements.

IX. Sensitivity Study

A sensitivity study was conducted to quantify the relationship each user-definable parameter had on the performance of the PHM algorithm. Filtering methods are very sensitive to posterior "tweaking" that can improve reported performance. In practice a training data set would be required to enable prior knowledge of reasonable user-definable parameters. To quantify the severity of incorrectly picking these parameters a cumulative beta was calculated to provide a single number that could represent the performance of the algorithm while user-definable parameters were varied. Larger values of cumulative beta sum indicate better performance of the algorithm.

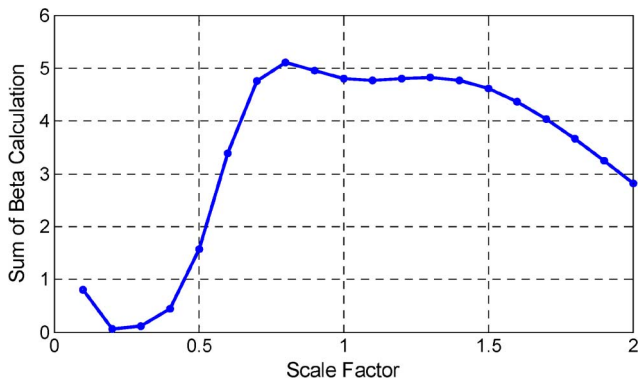

Fig. 31. Variation in the sum of the beta calculation for variations in the critical-threshold of state variable.

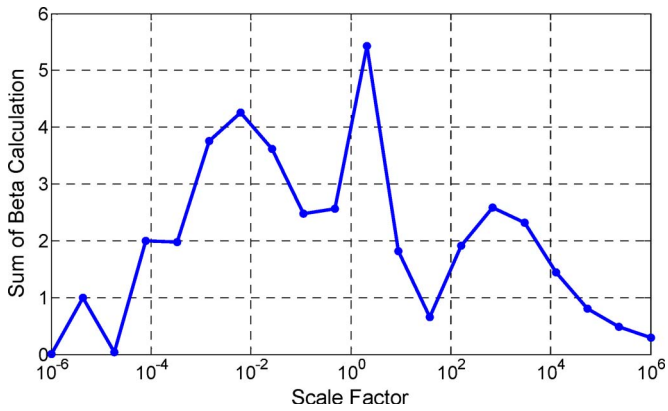

Fig. 32. Variation in the sum of beta calculation for variations in tunable the process noise parameter.

Parameter variations studied include: state variable failure threshold and measurement noise in the Kalman filter. State variable failure threshold is the value at which the system is deemed to have failed. The process noise is a user-definable parameter signifying the underlying noise in the measured process. Increasing the measurement noise makes the estimated resistance measurement smoother, but less reactive to error between predicted and actual state values. Fig. 31 shows the variation in the results of the algorithm when the critical value of the state variable was varied. Fig. 32 shows the cumulative beta with respect to the process noise.

The sensitivity study shows that underestimating the critical value of state variable can severely hurt the performance of the PHM algorithm. A physics-based understanding of the degradation mechanism and its relationship to system performance is critical for implementation of the PHM algorithm. The cumulative beta score is less sensitive to process noise and therefore was varied over a number of orders of magnitude. An incorrect selection of either critical threshold for state variable or the process noise will have an adverse effect on the performance of the PHM algorithm.

X. Risk-Based Decision Making

The practical result of predicting RUL is to make decisions. In the Bayesian framework used in this paper, critical decisions about future use and replacement of a component can be

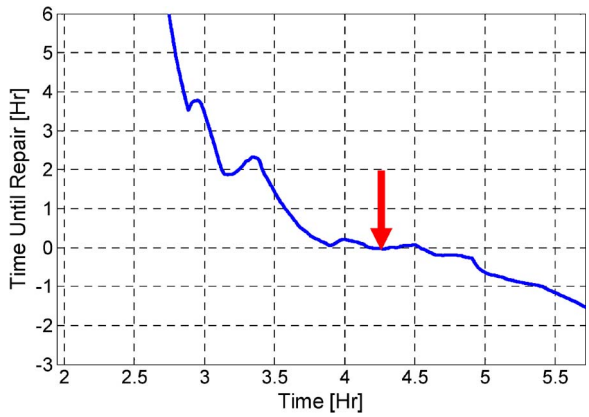

Fig. 33. Time to order replacement component calculation versus time, which demonstrates one method of statistically defendable decision making using estimates of RUL.

justified using statistics. In an ultrahigh reliability system, a critical decision is whether to replace a component. In high risk, mission critical systems for which this technique was designed, the maximum acceptable probability of failure is limited to 1%. This conservative restriction reflects the highly undesirable consequences of an unplanned failure.

The calculation to determine when to order a replacement part and schedule downtime for maintenance is based on the mean and standard deviation of the RUL prediction. In normally distributed data, the proportion of values within z standard deviations of the mean is

$$\text{proportion} = \text{erf}\left(\frac{z}{\sqrt{2}}\right) \tag{17}$$

where erf is the error function. A z value of 2.3263 represents the case where 98% of samples would be contained within $+/-2.3263\sigma$ standard deviations of the mean. One percent of the samples outside $+/-2.3263\sigma$ would fall on the negative side of the distribution, and the other 1% would fall on the positive side of the distribution. For predicting failures, we are only concerned with the negative side of the distribution or the 1% probability of failure. Using this approach, the appropriate time to order a replacement can be calculated. Assume that it takes 1 hour to order and receive a replacement component from the warehouse. Based on the predicted RUL, predicted RUL standard deviation, and a maximum acceptable probability of failure of 1%, the time until a replacement part should be reordered can be predicted by

$$t_{\text{order}} = \text{RUL}_{\text{prediction}} - 2.3263\sigma_{\text{RUL}} - t_{\text{leadtime}} \tag{18}$$

where σ_{RUL} is the standard deviation of the RUL, and t_{leadtime} is the lead time for receiving the component after placement of the order. This equation is implemented on the data for the vibration test and is shown in Fig. 33. The order for the replacement component is placed when the t_{order} parameter reaches a value of zero, indicated by a red arrow in Fig. 33.

XI. Summary and Conclusion

A framework for prognosis of area-array electronics has been developed based on state-space vectors from resistance spectroscopy measurements, Kalman filtering, and Bayesian PHM framework. The measured state variable has been related to the underlying damage state by correlating the resistance change to the plastic strain accrued in interconnects using nonlinear finite-element analysis. The strain-resistance relationship has been used to define the critical resistance failure threshold for the component. The Kalman filter was used to estimate the state variable, rate of change of the state variable, acceleration of the state variable, and to construct a feature vector. The estimated state-space parameters were used to extrapolate the feature vector into the future and predict the time-to-failure at which the feature vector will cross the failure threshold. This procedure was repeated recursively until the component failed. RUL was calculated based on the evolution of the state space feature vector. Standard PHM metrics were used to quantify the performance of the algorithm against the actual RUL. An example application to part replacement decisions for ultrahigh reliability systems was demonstrated. Finally, the techniques described in the paper were used to determine the correct time to order a replacement for the component being monitored.

References

[1] A. Steininger and C. Scherrer, "On the necessity of on-line-BIST in safety-critical applications-a case-study," in *29th Annu. Int. Symp. Fault-Tolerant Comput. Dig. Papers*, 1999, pp. 208–215.

[2] I. G. Harris and R. Tessier, "Testing and diagnosis of interconnect faults in cluster-based FPGA architectures," *IEEE Trans. Comput.-Aided Design Integr. Circuits Syst.*, vol. 21, no. 11, pp. 1337–1343, Nov. 2002.

[3] H. Hashempour, F. J. Meyer, and F. Lombardi, "Analysis and measurement of fault coverage in a combined ATE and BIST environment," *IEEE Trans. Instrum. Meas.*, vol. 53, no. 2, pp. 300–307, Apr. 2004.

[4] *Guidelines for Accelerated Reliability Testing of Surface Mount Solder Attachments*, IPC-SM-785, 1992.

[5] *JDEC Standard, Vibration at Variable Frequency*, JESD22-B103-B, 2002.

[6] V. Suthar and S. Dutt, "Efficient on-line interconnect testing in FPGAs with provable detectability for multiple faults," in *Proc. DATE*, 2006, pp. 1:1–1:6.

[7] P. Lall, N. Islam, K. Rahim, J. Suhling, and S. Gale, "Leading indicators-of-failure for prognosis of electronic and MEMS packaging," in *Proc. 54th Electron. Compon. Technol. Conf.*, Las Vegas, NV, Jun. 1–4, 2004, pp. 1570–1578.

[8] P. Lall, N. Islam, J. C. Suhling, and R. Darveaux, "Model for BGA and CSP reliability in automotive underhood applications," *IEEE Trans. Compon. Packag. Technol.*, vol. 27, no. 3, pp. 585–593, Sep. 2004.

[9] P. Lall, N. Islam, P. Choudhary, and J. Suhling, "Prognostication and health monitoring of leaded and lead free electronic and MEMS packages in harsh environments," in *Proc. 55th IEEE Electron. Compon. Technol. Conf.*, Orlando, FL, Jun. 1–3, 2005, pp. 1–9.

[10] P. Lall, P. Choudhary, S. Gupte, and J. Suhling, "Health monitoring for damage initiation & progression during mechanical shock in electronic assemblies," in *Proc. 56th IEEE Electron. Compon. Technol. Conf.*, San Diego, CA, May 30–Jun. 2, 2006, pp. 85–94.

[11] P. Lall, M. Hande, N. Singh, J. Suhling, and J. Lee, "Feature extraction and damage data for prognostication of leaded and leadfree electronics," in *Proc. 56th IEEE Electron. Compon. Technol. Conf.*, San Diego, CA, May 30–Jun. 2, 2006, pp. 718–727.

[12] P. Lall, N. Islam, K. Rahim, J. Suhling, and S. Gale, "Prognostics and health management of electronic packaging," *IEEE Trans. Compon. Packag. Technol.*, vol. 29, no. 3, pp. 666–677, Sep. 2006.

[13] P. Lall, P. Choudhary, S. Gupte, J. Suhling, and J. Hofmeister, "Statistical pattern recognition and built-in reliability test for feature extraction and health monitoring of electronics under shock loads," in *Proc. 57th Electron. Compon. Technol. Conf.*, Reno, NV, May 30–Jun. 1, 2007, pp. 1161–1178.

[14] P. Lall, M. Hande, C. Bhat, J. Suhling, and J. Lee, "Prognostics health monitoring (PHM) for prior-damage assessment in electronics equipment under thermo-mechanical loads," in *Proc. Electron. Compon. Technol. Conf.*, Reno, NV, May 29–Jun. 1, 2007, pp. 1097–1111.

[15] P. Lall, M. Hande, C. Bhat, N. Islam, J. Suhling, and J. Lee, "Feature extraction and damage-precursors for prognostication of lead-free electronics," *Microelectron. Reliab.*, vol. 47, no. 12, pp. 1907–1920, Dec. 2007.

[16] P. Lall, P. Choudhary, S. Gupte, and J. Suhling, "Health monitoring for damage initiation and progression during mechanical shock in electronic assemblies," *IEEE Trans. Compon. Packag. Technol.*, vol. 31, no. 1, pp. 173–183, Mar. 2008.

[17] P. Lall, M. Hande, C. Bhat, V. More, R. Vaidya, and J. Suhling, "Algorithms for prognostication of prior damage and residual life in lead-free electronics subjected to thermo-mechanical loads," in *Proc. 10th ITherm*, Orlando, FL, May 28–31, 2008, pp. 638–651.

[18] P. Lall, D. Iyengar, S. S. Shantaram, P. Gupta, D. Panchagade, and J. Suhling, "Keynote Presentation: Feature extraction and health monitoring using image correlation for survivability of leadfree packaging under shock and vibration," in *Proc. 9th EuroSIME*, Freiburg, Germany, Apr. 16–18, 2008, pp. 594–608.

[19] P. Lall, R. Lowe, and K. Goebel, "Resistance spectroscopy-based condition monitoring for prognostication of high reliability electronics under shock-impact," in *Proc. 59th Electron. Compon. Technol. Conf.*, San Diego, CA, 2009, pp. 1245–1255.

[20] P. Lall, R. Lowe, and J. Suhling, "Prognostication based on resistance-spectroscopy for high reliability electronics under shock-impact," in *Proc. ASME IMECE*, Lake Buena Vista, FL, Nov. 13–19, 2009, pp. 1–12.

[21] P. Lall, R. Lowe, and K. Goebel, "Particle filter models and phase sensitive detection for prognostication and health monitoring of leadfree electronics under shock and vibration," in *Proc. IEEE ECTC*, 2011, pp. 1097–1109.

[22] P. Lall, R. Lowe, and K. Goebel, "Extended Kalman filter models and resistance spectroscopy for prognostication and health monitoring of lead-free electronics under vibration," in *Proc. IEEE PHM*, 2011, pp. 1–12.

[23] J. Constable and C. Sahay, "Electrical resistance as an indicator of fatigue," *IEEE Trans. Compon., Hybrids, Manuf. Technol.*, vol. 15, no. 6, pp. 1138–1145, Dec. 1992.

[24] J. H. Constable, W. Butler, C. Huang, and J. M. Pitarresi, "CSP fatigue life predictions based on electrical resistance change," in *Proc. ASME InterPack*, Kauai, HI, Jul. 2001, pp. 1–7.

[25] G. C. Downes, "ASTRAEA T7—An architectural outline for system health management on civil UAVs," in *Proc. Inst. Eng. Technol. Conf. Auton. Syst.*, 2007, pp. 1–4.

[26] R. S. McCann and L. Spirkovska, "Human factors of integrated systems health management on next-generation spacecraft," in *Proc. 1st Int. Forum Integr. Syst. Health Eng. Manage. Aerosp.*, Nov. 7–10, 2005, pp. 1–18.

[27] K. A. Marko, J. V. James, T. M. Feldkamp, C. V. Puskorius, J. A. Feldkamp, and D. Roller, "Applications of neural networks to the construction of virtual sensors and model-based diagnostics," in *Proc. 29th ISATA*, 1996, pp. 133–138.

[28] J. Schauz, "Wavelet neural networks for EEG modeling and classification," Ph.D. dissertation, Georgia Inst. Technol., Atlanta, GA, 1996.

[29] J. Shiroishi, Y. Li, T. Liang, T. Kurfess, and S. Danyluk, "Bearing condition diagnostics via vibration and acoustic emissions measurements," *Mech. Syst. Signal Process.*, vol. 11, no. 5, pp. 693–705, Sep. 1997.

[30] H. Guzmán-Miranda, L. Sterpone, M. Violante, M. Aguirre, and M. Gutiérrez-Rizo, "Coping with the obsolescence of safety- or mission-critical embedded systems using FPGAs," *IEEE Trans. Ind. Electron.*, vol. 58, no. 3, pp. 814–821, Mar. 2011.

[31] D. Jarrell, D. Sisk, and L. Bond, "Prognostics and Condition Based Maintenance (CBM) a scientific crystal ball," presented at the Int. Congr. Advanced Nuclear Power Plants (ICAPP), Hollywood, FL, Jun., 2002, Paper 194.

[32] T. E. Munns and R. M. Kent, "Structural health monitoring: Degradation mechanism and system requirements," in *Proc. Digit. Avionics Syst. Conf.*, 2000, vol. 2, pp. 6C2/1–6C2/8.

[33] C. Baldwin, J. Kiddy, T. Salter, P. Chen, and J. Niemczuk, "Fiber optic structural health monitoring system: Rough sea trials testing of the RV triton," in *Proc. MTS/IEEE Oceans*, Oct. 2002, vol. 3, pp. 1807–1814.

[34] P. C. Chang, A. Flatau, and S. C. Liu, "Review paper: Health monitoring of civil infrastructure," *Struct. Health Monitor.*, vol. 2, no. 3, pp. 257–267, Sep. 2003.

[35] B. Lu and V. Gungor, "Online and remote motor energy monitoring and fault diagnostics using wireless sensor networks," *IEEE Trans. Ind. Electron.*, vol. 56, no. 11, pp. 4651–4659, Nov. 2009.

[36] L. Frosini and E. Bassi, "Stator current and motor efficiency as indicators for different types of bearing faults in induction motors," *IEEE Trans. Ind. Electron.*, vol. 57, no. 1, pp. 244–251, Jan. 2010.

[37] R. Romary, S. Jelassi, and J. F. Brudny, "Stator-interlaminar-fault detection using an external-flux-density sensor," *IEEE Trans. Ind. Electron.*, vol. 57, no. 1, pp. 237–243, Jan. 2010.

[38] Y. Xiong, X. Cheng, Z. Shen, C. Mi, H. Wu, and V. Garg, "Prognostic and warning system for power-electronic modules in electric, hybrid electric and fuel-cell vehicles," *IEEE Trans. Ind. Electron.*, vol. 55, no. 6, pp. 2268–2276, Jun. 2008.

[39] A. Y. Goharrizi and N. Sepehri, "A wavelet-based approach to internal seal damage diagnosis in hydraulic actuators," *IEEE Trans. Ind. Electron.*, vol. 57, no. 5, pp. 1755–1763, May 2010.

[40] D. Barke and W. K. Chiu, "Structural health monitoring in the railway industry: A review," *Struct. Health Monitor.*, vol. 4, no. 1, pp. 81–93, Mar. 2005.

[41] R. Kalman, "A new approach to linear filtering and prediction problems," *Trans. ASME, J. Basic Eng.*, vol. 82D, pp. 35–45, 1960.

[42] P. Zarchan and H. Musoff, *Fundamentals of Kalman Filtering: A Practical Approach*, vol. 190, *Progress in Astronautics and Aeronautics*. Washington, DC: AIAA, 2000.

[43] Y. Bar-Shalom, X.-R. Li, and K. Thiagalingam, *Estimation with Applications to Tracking and Navigation*. Hoboken, NJ: Wiley, 2001.

[44] S. Solomou, *Economic Cycles*. Manchester, U.K.: Manchester Univ. Press, 1998.

[45] E. Manla, A. Nasiri, C. Rentel, and M. Hughes, "Modeling of zinc bromide energy storage for vehicular applications," *IEEE Trans. Ind. Electron.*, vol. 57, no. 2, pp. 624–632, Feb. 2010.

[46] M. Charkhgard and M. Farrokhi, "State-of-charge estimation for Lithium-Ion batteries using neural networks and EKF," *IEEE Trans. Ind. Electron.*, vol. 57, no. 12, pp. 4178–4187, Dec. 2010.

[47] A. Akrad, M. Hilairet, and D. Diallo, "Design of a fault-tolerant controller based on observers for a PMSM drive," *IEEE Trans. Ind. Electron.*, vol. 58, no. 4, pp. 1416–1427, Apr. 2011.

[48] K. D. Herring and F. Seiler, *Evaluation of an Estimator for Real-Time Missile Tracking*. Fort Belvoir, VA: Defense Tech. Inf. Center, 1974.

[49] D. M. Bevly and B. Parkinson, "Cascaded Kalman filters for accurate estimation of multiple biases, dead-reckoning navigation, and full state feedback control of ground vehicles," *IEEE Trans. Control Syst. Technol.*, vol. 15, no. 2, pp. 199–208, Mar. 2007.

[50] R. C. Hayward, D. Gebre-Egziabher, M. Schwall, J. D. Powell, and J. Wilson, "Inertially aided GPS based Attitude Heading Reference System (AHRS) for general aviation aircraft," in *Proc. ION-GPS Conf.*, 1997, pp. 1415–1424.

[51] G. F. Gueler, "Modelling, design and analysis of an autopilot for submarine vehicles," *Int. Shipbuild. Progr.*, vol. 36, no. 405, pp. 51–85, 1989.

[52] J. G. Balchen, N. A. Jenssen, E. Mathisen, and S. Sælid, "A dynamic positioning system based on Kalman filtering and optimal control," *Model. Identification Control*, vol. 1, no. 3, pp. 135–163, 1980.

[53] S. Won, W. Melek, and F. Golnaraghi, "A Kalman/particle filter-based position and orientation estimation method using a position sensor/inertial measurement unit hybrid system," *IEEE Trans. Ind. Electron.*, vol. 57, no. 5, pp. 1787–1798, May 2010.

[54] T. D. Batzel and D. C. Swanson, "Prognostic health management of aircraft power generators," *IEEE Trans. Aerosp. Electron. Syst.*, vol. 45, no. 2, pp. 473–482, Apr. 2009.

[55] D. Swanson, M. Spencer, and S. Arzoumaniana, "Prognostic modeling of crack growth in a tensioned steel band," *Mech. Syst. Signal Process.*, vol. 14, no. 5, pp. 789–803, Sep. 2000.

[56] D. C. Swanson, "A general prognostic tracking algorithm for predictive maintenance," in *Proc. IEEE Aerosp. Conf.*, 2001, vol. 6, pp. 2971–2977.

[57] B. Saha and K. Goebel, "Modeling Li-ion battery capacity depletion in a particle filtering framework," in *Proc. Annu. Conf. Prognost. Health Manage. Soc.*, San Diego, CA, 2009a, pp. 1–10.

[58] B. Saha, "Prognostics methods for battery health monitoring using a Bayesian framework," *IEEE Trans. Instrum. Meas.*, vol. 58, no. 2, pp. 291–296, Feb. 2009.

[59] R. Darveaux, C. Reichman, and N. Islam, "Interface failure in lead free solder joints," in *Proc. 56th Electron. Compon. Technol. Conf.*, San Diego, CA, 2006, pp. 906–917.

[60] D. Y. R. Chong, F. X. Che, J. H. L. Pang, K. Ng, J. Y. N. Tan, and P. T. H. Low, "Drop impact reliability testing for lead-free and lead-based soldered IC packages," *Microelectron. Reliab.*, vol. 46, no. 7, pp. 1160–1171, Jul. 2006.

[61] Y. G. Bagul, I. Zeid, and S. V. Kamarthi, "A framework for prognostics and health management of electronic systems," in *Proc. IEEE Aerosp. Conf.*, Mar. 1–8, 2008, pp. 1–9.

[62] M. Schwabacher and K. Goebel, "A survey of artificial intelligence for prognostics," in *Proc. AAAI Fall Symp.*, 2007, pp. 107–114.

[63] M. E. Orchard and G. J. Vachtsevanos, "A particle filtering approach for on-line failure prognosis in a planetary carrier plate," *Int. J. Fuzzy Logic Intell. Syst.*, vol. 7, no. 4, pp. 221–227, Dec. 2007.

[64] B. Saha and K. Goebel, "Uncertainty management for diagnostics and prognostics of batteries using Bayesian techniques," in *Proc. IEEE Aerosp. Conf.*, Big Sky, MT, Mar. 1–8, 2008, pp. 1–10.
[65] S. Engel, "PHM engineering perspectives, challenges and 'crossing the valley of death'," in *Proc. Annu. Conf. Prognost. Health Manage. Soc.*, San Diego, CA, 2009, pp. 1–21.
[66] A. Saxena, J. Celaya, B. Saha, and K. Goebel, "Evaluating algorithm performance metrics tailored for prognostics," in *Proc. IEEE Aerosp. Conf.*, 2009a, pp. 1–13.
[67] A. Saxena, J. Celaya, B. Saha, S. Saha, and K. Goebel, "On applying the prognostics performance metrics," in *Proc. Annu. Conf. PHM Soc.*, San Diego, CA, 2009b, vol. 1.
[68] A. Saxena, J. Celaya, B. Saha, S. Saha, and K. Goebel, "Evaluating algorithm performance metrics tailored for prognostics," in *Proc. IEEE Aerosp. Conf.*, Big Sky, MT, Mar. 2008a, pp. 1–11.
[69] A. Saxena, J. Celaya, E. Balaban, K. Goebel, B. Saha, S. Saha, and M. Schwabacher, "Metrics for evaluating performance of prognostic techniques," in *Proc. Int. Conf. Progn. Health Manage.*, Denver, CO, Oct. 2008b, pp. 1–17.

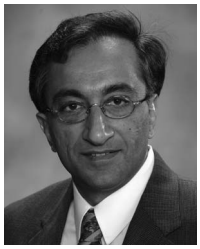

Pradeep Lall (M'93–SM'08–F'12) received the B.E. degree in mechanical engineering from the Delhi College of Engineering, Delhi, India, in 1988, the M.S. and Ph.D. degrees in mechanical engineering from the University of Maryland, College Park, in 1989 and 1993, respectively, and the M.B.A. degree from Kellogg School of Management, Northwestern University, Evanston, IL, in 2002.

He is the Thomas Walter Professor with Department of Mechanical Engineering and Director of the NSF Center for Advanced Vehicle and Extreme Environment Electronics at Auburn University, Auburn, AL. He has 10 years of industry experience. He was previously with Motorola's Wireless Technology Center. He has published extensively in the area of electronic packaging with emphasis on modeling and predictive techniques. He is author and coauthor of 2 books, 13 book chapters, and over 270 journal and conference papers in the field of electronic packaging with emphasis on design, modeling and predictive techniques.

Dr. Lall is a Fellow of the IEEE (2012) and a Fellow of the ASME (2008). He is a member of the National Academies Committee on Electronic Vehicle Controls and Unintended Acceleration. Dr. Lall is a member of the Beta Gamma Sigma honorary Society. He is recipient of the Samuel Ginn College of Engineering Senior Faculty Research Award and three-Motorola Outstanding Innovation Awards. He has received five Motorola Engineering Awards and four Publication Awards. He holds three U.S. Patents. He is a Six-Sigma Black-Belt in Statistics. He is the founding faculty advisor for the SMTA student chapter at Auburn University and member of the editorial advisory board for SMTA Journal. He is a member of the IEEE Reliability Society Advisory Committee. He is the Vice-Chair of the ASME Congress Steering Committee. Dr. Lall is the Associate Editor of the ASME Journal of Electronic Packaging, and theIEEE TRANSACTIONS ON COMPONENTS AND PACKAGING TECHNOLOGIES.

Ryan Lowe is a doctoral candidate in the mechanical engineering Department at Auburn University, Auburn, AL, and researcher at the NSF-CAVE3 Electronics Research Center.

His research interests include prognostic health management for electrical components subjected to drop, shock, and vibration environments. Recent accolades for his work include a best paper and best poster award. Prior to attending graduate school he worked at Hubbell Power Systems in Columbia, SC as the manager of continuous improvement.

Kai Goebel received the degree of Diplom-Ingenieur from the TechnischeUniversität München, München, Germany, in 1990. He received the M.S. and Ph.D. degrees from the University of California at Berkeley, in 1993 and 1996, respectively.

He worked at General Electric's Corporate Research Center in Niskayuna, NY, from 1997 to 2006 as a senior research scientist. He has carried out applied research in the areas of artificial intelligence, soft computing, and information fusion. His research interest lies in advancing these techniques for real-time monitoring, diagnostics, and prognostics. He holds 11 patents and has published more than 150 papers in the area of systems health management. He is a Senior Scientist at NASA Ames Research Center where he leads the Diagnostics and Prognostics groups in the Intelligent Systems Division. In addition, he directs the Prognostics Center of Excellence, and he is the Associate Principal Investigator for Prognostics of NASA's Integrated Vehicle Health Management Program.